

Article

Exploiting Deep Matching and SAR Data for the Geo-Localization Accuracy Improvement of Optical Satellite Images

Nina Merkle ^{1,*}, Wenjie Luo ², Stefan Auer ¹, Rupert Müller ¹ and Raquel Urtasun ²

¹ German Aerospace Center (DLR), Remote Sensing Technology Institute, 82234 Wessling, Germany; stefan.auer@dlr.de (S.A.); rupert.mueller@dlr.de (R.M.)

² Department of Computer Science University of Toronto, Toronto, ON M5S 3G, Canada; wenjie@cs.toronto.edu (W.L.); urtasun@cs.toronto.edu (R.U.)

* Correspondence: nina.merkle@dlr.de; Tel.: +49-8153-28-2165

Academic Editors: Qi Wang, Nicolas H. Younan, Carlos López-Martínez and Prasad S. Thenkabail

Received: 20 March 2017; Accepted: 29 May 2017; Published: 10 June 2017

Abstract: Improving the geo-localization of optical satellite images is an important pre-processing step for many remote sensing tasks like monitoring by image time series or scene analysis after sudden events. These tasks require geo-referenced and precisely co-registered multi-sensor data. Images captured by the high resolution synthetic aperture radar (SAR) satellite TerraSAR-X exhibit an absolute geo-location accuracy within a few decimeters. These images represent therefore a reliable source to improve the geo-location accuracy of optical images, which is in the order of tens of meters. In this paper, a deep learning-based approach for the geo-localization accuracy improvement of optical satellite images through SAR reference data is investigated. Image registration between SAR and optical images requires few, but accurate and reliable matching points. These are derived from a Siamese neural network. The network is trained using TerraSAR-X and PRISM image pairs covering greater urban areas spread over Europe, in order to learn the two-dimensional spatial shifts between optical and SAR image patches. Results confirm that accurate and reliable matching points can be generated with higher matching accuracy and precision with respect to state-of-the-art approaches.

Keywords: geo-referencing; multi-sensor image matching; Siamese neural network; satellite images; synthetic aperture radar

1. Introduction

1.1. Background and Motivation

Data fusion is important for several applications in the fields of medical imaging, computer vision or remote sensing, allowing the collection of complementary information from different sensors or sources to characterize a specific object or an image. In remote sensing, the combination of multi-sensor data is crucial, e.g., for tasks such as change detection, monitoring or assessment of natural disasters. The fusion of multi-sensor data requires geo-referenced and precisely co-registered images, which are often not available.

Assuming the case of multi-sensor image data where one of the images exhibits a higher absolute geo-localization accuracy, image registration techniques can be employed to improve the localization accuracy of the second image. Images captured by high resolution synthetic aperture radar (SAR) satellites like TerraSAR-X [1] exhibit an absolute geo-localization accuracy in the order of a few decimeters or centimeter for specific targets [2]. Such accuracy is mainly due to the availability of precise orbit information and the SAR imaging principle. Radar satellites have active sensors onboard

(emitting electromagnetic signals) and capture images day and night independently from local weather conditions. The principle of synthetic aperture radar relates to collecting backscattered signal energy for ground objects along the sensor flight path and compressing the signal energy in post-processing for a significant increase of the spatial resolution [4]. The visual interpretation of SAR images is a challenging task [5]: the SAR sensor looks sideways (angle typically between 25° to 60° with respect to nadir direction) to be able to solve ambiguities in azimuth related to the targets on ground.

Contrary to radar systems that measure the signal backscattered from the reflecting target to the sensor, optical satellite sensors are passive systems that measure the sunlight reflected from ground objects with a strong dependence on atmospheric and local weather conditions such as cloud and haze. Due to a different image acquisition concept with respect to SAR satellites (active vs. passive sensor), the location accuracy of optical satellites also depends on a precise knowledge of the satellite orientation in space. Inaccurate measurements of the attitude angles in space are the main reason for a lower geo-localization accuracy of optical satellite data. For example the absolute geo-localization accuracy of images from optical satellites like Worldview-2, PRISM or QuickBird ranges from 4 to 30 m. TerraSAR-X images may therefore be employed to improve the localization accuracy of spatially high resolution optical images with less than 5 m ground resolution.

The aim of enhancing the geo-localization accuracy of optical images could be achieved by employing ground control points (GCPs). GCPs can be extracted from high resolution reference images, e.g., from TerraSAR-X, to correctly model the generation process of optical images from the focal plane location of the instrument pixel to the Earth surface location in terms of Earth bound coordinate frames. In Reinartz et al. [3] promising results are archived by using GCPs extracted from high precision orthorectified TerraSAR-X data. Nevertheless, the problem of multi-sensor image to image registration is challenging, and in the specific the precise registration of images from radar and optical sensors is an open problem.

Due to the different acquisition concepts (SAR: synthetic aperture with distance measurements; optical: perspective projection), viewing perspectives (off-nadir; usually near-nadir), wavelengths (radar signal wavelength in cm; optical wavelength in nm) and the speckle effect in SAR images, it is difficult to find complementary features or reliable similarity measures when comparing optical and SAR images. More precisely, the sideways-looking acquisition of SAR sensors causes typical geometric distortion effects (layover, foreshortening) and shadowing for 3D objects such as buildings or trees. These effects have a strong influence on the appearance of all objects above the ground level in SAR images. As a consequence, the boundary of an elevated object in a SAR image does not fit the object boundary in the optical image, even if the imaging perspective is the same for both sensors. Additionally, the different wavelengths measured by the two kinds of sensors lead to different radiometric properties in the optical and SAR images. This is due to the fact that the response of an object depends on the signal properties (wavelength, polarization), the surface properties (roughness, randomness of local reflectors and reflectance properties) and sensor perspective. The same object may therefore appear with high intensity for one sensor and with low intensity in another. The speckle effect further complicates the human and automatic interpretation of SAR imagery and, hence, the matching of optical and SAR images. As an example, Figure 1 shows the difference of an optical and a high resolution SAR image for a selected scene containing man-made structures and vegetation.



Figure 1. Visual comparison of an optical (**top**) and SAR image (**bottom**) acquired over the same area. Both images have a ground sampling distance of 1.25 m.

1.2. Related Work

To improve the absolute geo-location accuracy of optical satellite images using SAR images as reference, the above-mentioned problems for SAR and optical image registration need to be dealt with. Different research studies investigated the geo-localization accuracy improvement of optical satellite images based on SAR reference data, e.g., [3,6,7]. The related approaches rely on suitable image registration techniques, which are tailored to the problem of optical and SAR images matching.

The aim of image registration is to estimate the optimal geometric transformation between two images. The most common multi-modal image registration approaches can be divided into two categories. The first category comprises intensity-based approaches, where a transformation between the images can be found by optimizing the corresponding similarity measure. Influenced by the field of medical image processing, similarity measures like normalized cross-correlation [8], mutual information [9,10], cross-cumulative residual entropy [11] and the cluster reward algorithm [12] are frequently used for SAR and optical image registration. A second approach is based on local frequency information and a confidence-aided similarity measure [13]. Li et al. [14] and Ye et al. [15] introduced similarity measures based on the histogram of oriented gradients and the histogram of oriented phase congruency, respectively. However, these approaches are often computationally expensive, suffer from the different radiometric properties of SAR and optical images and are sensitive to speckle in the SAR image.

The second category comprises feature-based approaches, which rely on the detection and matching of robust and accurate features from salient structures. Feature-based approaches are less sensitive to radiometric differences of the images, but have problems in the detection of robust features from SAR images due to the impact of speckle. Early approaches are based on image features like lines [16], contours [17,18] or regions [19]. A combination of different features (points, straight lines, free-form curves or areal regions) is investigated in [20]. The approach shows good performance for the registration of optical and SAR images, but the features from the SAR images have to be selected manually. As the matching between optical and SAR images usually fails using the scale-invariant feature transform (SIFT), Fan [21] introduced a modified version of the algorithm. With the improved SIFT, a fine registration for coarsely-registered images can be achieved, but the approach fails for image pairs with large geometric distortions. To find matching points between area features, a level set segmentation-based approach is introduced in [22]. This approach is limited to images that contain sharp edges from runways, rivers or lakes. Sui et al. [23] and Xu et al. [22] propose iterative matching procedures to overcome the problem of misaligned images caused by imprecise extracted features. In [23], an iterative Voronoi spectral point matching between the line-intersection is proposed, which depends on the presence of salient straight line features in the images.

Other approaches try to overcome the drawbacks of intensity and feature-based approaches by combining them. A global coarse registration using mutual information on selected areas (no dense urban and heterogeneous areas) followed by a fine local registration based on linear features is proposed in [24]. As a drawback, the method highly depends on the coarse registration. If the coarse registration fails, the fine registration will be unreliable.

Besides classical registration approaches, a variety of research studies indicate the high potential of deep learning methods for different applications in remote sensing, such as classification of hyperspectral data [25–27], enhancement of existing road maps [28,29], high-resolution SAR image classification [30] or pansharpening [31]. In the context of image matching, deep matching networks were successfully trained for tasks such as stereo estimation [32,33], optical flow estimation [34,35], aerial image matching [36] or ground to aerial image matching [37]. In [38], a deep learning-based method is proposed to detect and match multiscale keypoints with two separated networks. While the detection network is trained on multiscale patches to identify regions including good keypoints, the description network is trained to match extracted keypoints from different images.

Most of the deep learning image matching methods are based on a Siamese network architecture [39]. The basic idea of these methods is to train a neural network that is composed of two parts: the first part, a Siamese or pseudo-Siamese network, is trained to extract features from image patches, while the second part is trained to measure the similarity between these features. Several types of networks showed a high potential for automatic feature extraction from images, e.g., stacked (denoising) autoencoders [40], restricted Boltzmann machines [41] or convolutional neural networks (CNNs) [42]. From these networks, CNNs have been proven to be efficient for feature extraction and have been successfully trained for image matching in [32,33,36–38,43–45]. A similarity measure, the L_2 distance [45] or the dot product [32,33], is applied on a fully-connected network [43,44]. The input of the network can be single-resolution image patches [36,43,45], multi-resolution patches [44] or patches that differ in size for the left and right branch of the Siamese network [32,44].

Summarizing, we are tackling the task of absolute geo-location accuracy improvement of optical satellite images by generating few, but very accurate and reliable matching points between SAR and optical images with the help of a neural network. These points serve as input to improve the sensor models for optical image acquisitions. The basis of the approach is a Siamese network, which is trained to learn the spatial shift between optical and SAR image patches. Our network is trained on selected patches where the differences are mostly radiometric, as we try to avoid geometrical ones. The patches for training are semi-manually extracted from TerraSAR-X and PRISM image pairs that capture larger urban areas spread over Europe.

2. Deep Learning for Image Matching

Our research objective is to compute a subset of very accurate and reliable matching points between SAR and optical images. Common optical and SAR image matching approaches are often not applicable to a wide range of images acquired over different cities or at different times of the year. This problem can be handled using a deep learning-based approach. Through training a suitable neural network on a large dataset containing images spread over Europe and acquired at different times of the year, the network will learn to handle radiometric changes of an object over time or at different locations in Europe. To avoid geometrical differences between the SAR and optical patches, we focus our training on patches containing flat surfaces such as streets or runways in rural areas. This is not a strong restriction of our approach as these features frequently appear in nearly every satellite image.

Inspired by the successful use of Siamese networks for the task of image matching, we adopt the same architecture. A Siamese network consists of two parallel networks, which are connected at their output node. If the parameters between the two networks are shared, the Siamese architecture provides the advantage of consistent predictions. As both network branches compute the same function, it is ensured that two similar images will be mapped to a similar location in the feature space. Our Siamese network consists of two CNNs. In contrast to fully-connected or locally-connected networks, a CNN uses filters, which are deployed for the task of feature extraction. Using filters instead of full or local connections reduces the amount of parameters within the network. Less parameters lead to a speed increase in the training procedure and a reduction in the amount of required training data and, hence, reduce the risk of overfitting.

In comparison to common deep learning-based matching approaches, our input images are acquired from different sensors with different radiometric properties. Due to speckle in SAR images, the pre-processing of the images plays an important role during training and for the matching accuracy and precision of the results. Our dataset contains images with a spatial resolution of 2.5 m, and therefore exhibit a lower level of detail in the images compared to the ones used in [32,43–45]. In order to increase the probability of the availability of salient features in the input data, we use large input patches with at least a size of 201×201 pixels. The mentioned problems require a careful selection of the network architecture to find the right trade-off between the number of parameters, the number of layers and, more importantly, the receptive field size.

2.1. Dilation

In the context of CNNs, the receptive field refers to the part of the input patches, having an impact on the output of the last convolutional layer. To achieve the whole input patch having an impact on our network output, a receptive field size of 201×201 pixels is desired. Standard ways to increase the receptive field size are strided convolutions or pooling (downsampling) layers inside the neural network. Here, the word stride refers to the distance between two consecutive positions of the convolution filters. This would introduce a loss of information as these approaches reduce the resolution of the image features. In contrast, dilated convolutions [46] systematically aggregate information through an exponential growth of the receptive without degradation in resolution. The dilated convolution $*_d$ at a given position p in the image F is defined as:

$$(F *_d k)(p) = \sum_{m=-r}^r F(p - d \cdot m)k(m), \quad (1)$$

where k denotes the kernel/filter with size $(2r + 1) \times (2r + 1)$ and d denotes the dilation factor. Instead of looking at local $(2r + 1) \times (2r + 1)$ regions as in the case of standard convolutions, dilated convolutions look at $[d \cdot (2r + 1)] \times [d \cdot (2r + 1)]$ surrounding regions, which lead to an expansion of the receptive field size. Beyond this, dilated convolutions have the same number of network parameters compared to their convolution counterpart.

2.2. Network Architecture

Our matching network is composed of a feature extraction network (a Siamese network) followed by a layer to measure the similarity of the extracted features (the dot product layer). An overview of the network architecture is depicted on the left side of Figure 2. The inputs of the left and right branches of the Siamese network are an optical (left) and a SAR (right) reference image, respectively. The weights of the two branches can be shared (Siamese architecture) or partly shared (pseudo-Siamese architecture).

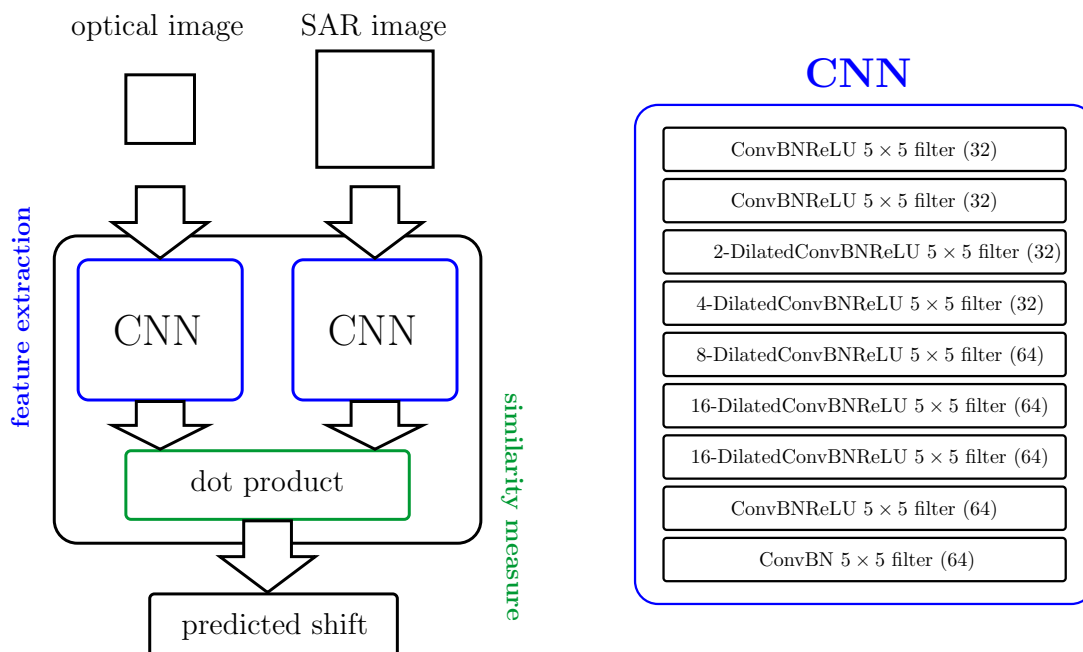


Figure 2. Network architecture (left) and a detailed overview of the convolutional layers (right). Abbreviations: convolutional neural network (CNN), convolution (Conv), batch normalization (BN) and rectified linear unit (ReLU).

Each layer of the network consists of a spatial convolution (Conv), a spatial batch normalization (BN) [47] and a rectified linear unit (ReLU). The purpose of the convolution layers is to extract spatial features from the input data through trainable filters. The complexity of the features extracted by the layers increases along with the depth. A normalization of the input data is often used as a pre-processing step to increase the learning speed and the performance of the network. By passing the input through the different layers of the network, the distribution of each single layer input changes. Therefore, BN is used in every layer of the network to ensure the consistency in the distribution of the layer inputs, as it provides a form of regularization and reduces the dependency of the network performance on the initialization of the weights. Non-linear activation functions like ReLUs are needed to introduce nonlinearities into the network (otherwise the network can only model linear functions). An Advantage of ReLUs compared to other activation function is a more efficient and faster training of the network.

We removed the ReLU from the last layer to preserve the information encoded in the negative values. In all layers convolutions with a filter size of 5×5 pixels are employed. To overcome the problem of our relatively large input patch size, we adopt dilation convolutions [46] for the layers three to seven with a dilation factor d of 2, 4, 8 and 16 for the last two layers. This setup leads to the desired receptive field size of 201×201 pixels. The number of filters used in layer one to four is 32 and for the others is 64. The overall output is a predicted shift of the optical image within the SAR reference patch

and is computed by taking the dot product of the output of the two branches. A detailed overview of one branch of the Siamese network is the depicted on the right side of Figure 2.

2.3. SAR Image Pre-Processing

We use the probabilistic patch-based (PPB) filter proposed in [48] for the pre-processing of the SAR images. This filter is developed to suppress speckle in SAR images by adapting the non-local mean filter by Buades et al. [49] to SAR images. The idea of the non-local mean filter is to estimate the filtered pixel value as the weighted average over all pixels in the image. The weights are measuring the similarity between the pixel values of a patch Δ_s centred around a pixel s and the pixel values of a patch Δ_t centred around a pixel t . The similarity between two patches is estimated through their Euclidean distance. In [48], the noise distribution is modelled using the weighted maximum likelihood estimator, in which the weights express the probability that two patches centred around the pixels s and t have the same noise distribution in a given image. The results of applying this filter and a comparison between SAR and optical patches are shown in Figure 3.

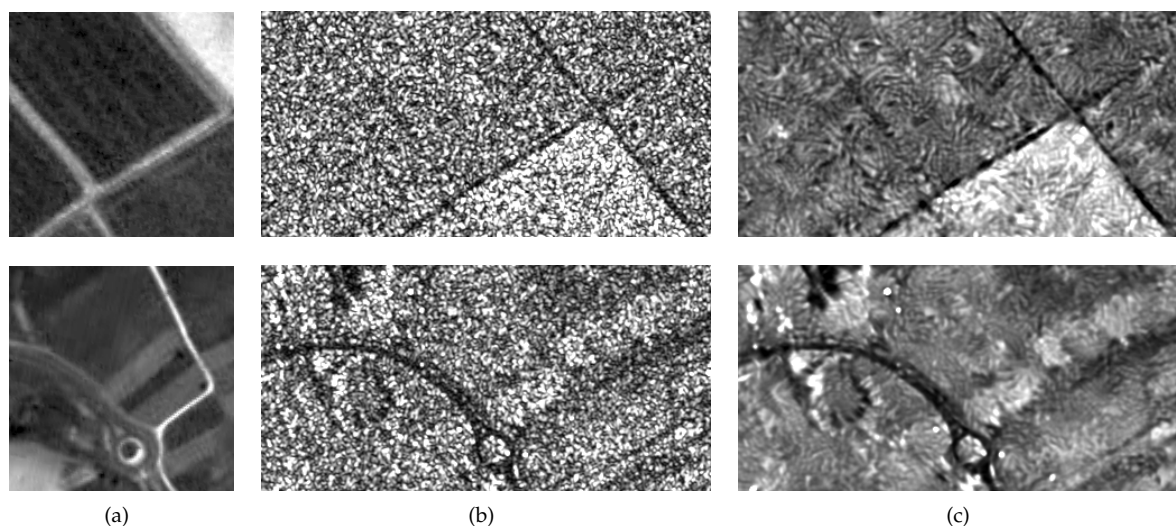


Figure 3. Visual comparison between optical (a), SAR (b) and despeckled SAR patches (c).

2.4. Matching Point Generation

We generate the matching points by training the network over a large dataset of optical and SAR image patch pairs, which have been manually co-registered. More precisely, the network is trained with smaller left image patches cropped from optical images and larger right image patches cropped from SAR images. Note that given a fixed size $b \times h$ of the left image patch L , the output of the network will depend on the size of the right image patch. The right image patch R has the size $(b + s) \times (h + s)$, where s defines the range over which we perform our search. The output of the network is a two-dimensional scoring map with size $(s + 1) \times (s + 1)$ over the search space S with size $(b + s) \times (h + s)$.

The scoring map s_i for the i -th input image pair contains a similarity score $s_{i,j}$ for each location $q_{i,j}$ in the search space ($j \in J = \{1, \dots, |S|\}$, where $|S|$ is the cardinality of S). The search space index J is indexing the two-dimensional search space, where each position $q_{i,j}$ in S corresponds to a specific two-dimensional shift of the left optical patch with respect to the larger SAR patch.

To get the similarity scores for every image pair, we first compute the feature vector f_i for the i -th optical training patch and the feature matrix h_i for the corresponding i -th SAR patch. The feature vector f_i is the output of the left network branches and has a dimension of 64 (as the last convolution layer has 64 filters). The feature matrix h_i is the output of the right network branch with a dimension

of $|S| \times 64$ and is composed of the feature vectors $h_{i,j}$ for each location in the search space. We then compute the similarity of the features vectors f_i and $h_{i,j}$ for every position $q_{i,j} \in S$.

To measure the similarity between the two vectors, we use the dot product and obtain the similarity scores $s_{i,j} = f_i \cdot h_{i,j}$ for all $j \in J$. A high value of $s_{i,j}$ indicates a high similarity between the two vectors f_i and $h_{i,j}$ at location $q_{i,j}$ (which is related to a two-dimensional pixel shift). In other words, a high similarity score $s_{i,j}$ indicates a high similarity between the i -th optical patch and the i -th SAR patch at location $q_{i,j}$ in our search space. To get a normalized score over all locations within the search space, we apply the soft-max function at each location $q_{i,j} \in S$:

$$\tilde{s}_{i,j} = \frac{\exp(s_{i,j})}{\sum_{j \in J} \exp(s_{i,j})}. \quad (2)$$

This function is commonly used for multi-class classification problems to compute the probability that a certain training patch belongs to a certain class. In our case, the normalized score $\tilde{s}_{i,j}$ can be interpreted as a probability for the specific shift, which corresponds to location $q_{i,j}$ with index j . Thus, the output of our network (the normalized score map) can be seen as a probability distribution with a probability for every location (shift) of the optical patch within the SAR image patch.

By treating the problem as a multi-class classification problem, where the different classes represent the possible shifts of an optical patch with respect to a larger SAR patch, we train our network by minimizing the cross entropy loss:

$$\min_w \sum_{i \in I, j \in J} p_{\text{gt}}(q_{i,j}) \log p_i(q_{i,j}, w) \quad (3)$$

with respect to the weights w , which parametrize our network. Here, $p_i(q_{i,j}, w)$ is the predicted score for sample i at location $q_{i,j}$ in our search space, and p_{gt} is the ground truth target distribution. Instead of a delta function with non-zero probability mass only at the correct location $q_{i,j} = q_i^{\text{gt}}$, we are using a soft ground truth distribution, which is centred around the ground truth location. Therefore, we set p_{gt} to be the discrete approximation of the Gaussian function (with $\sigma = 1$) in an area around q_i^{gt} :

$$p_{\text{gt}}(q_{i,j}) = \begin{cases} \frac{1}{2\pi} \cdot e^{-\frac{\|q_{i,j} - q_i^{\text{gt}}\|_2^2}{2}} & \text{if } \|q_{i,j} - q_i^{\text{gt}}\|_2 < 3 \\ 0 & \text{otherwise} \end{cases}, \quad (4)$$

where $\|\cdot\|_2$ denotes the L_2 (Euclidean) distance. We use stochastic gradient descent with Adam [50] to minimize our loss function (3) and, hence, to train our network to learn the matching between optical and SAR patches.

After training, we keep the learned parameters w fixed and decompose the network into two parts: the feature extractor (CNN) and the similarity measure (dot product layer). As the feature extractor is convolutional, we can apply the CNN on images with an arbitrary size. Thus, during the test time, we first give an optical patch as input to the CNN and compute the feature vector f . Then we consider a larger SAR patch which covers the desired search space, and compute the feature matrix h . Afterwards, we use the dot product layer to compute the normalized score map from f and h (in the same way as for the training step). Applying this strategy, we can compute a matching score between optical patches with arbitrary size and SAR images over an arbitrary search space. We obtain the matching points (predicted shifts) by picking for every input image pair the points with the highest value (highest similarity between optical and SAR patch) within the corresponding search space.

2.5. Geo-Localization Accuracy Improvement

The inaccuracy of the absolute geo-localization of the optical satellite data in the geo-referencing process arises mainly from inaccurate measurements of the satellite attitude and thermally-affected mounting angles between the optical sensor and the attitude measurement unit. This insufficient pointing knowledge leads to local geometric distortions of orthorectified images caused by the height variations of the Earth's surface. To achieve higher geometric accuracy of the optical data, ground control information is needed to adjust the parameters of the physical sensor model. We are following the approach described in [51] to estimate the unknown parameters of the sensor model from GCPs by iterative least squares adjustment. In order to get a reliable set of GCP, different levels of point filtering and blunder detection are included in the processing chain. In contrast to [51], where the GCPs are generated from an optical image, we are using the matching points generated by our network.

3. Experimental Evaluation and Discussion

To perform our experiments, we generated a dataset out of 46 orthorectified optical (PRISM) and radar (TerraSAR-X acquired in stripmap mode) satellite image pairs acquired over 13 city areas in Europe. The images include suburban, industrial and rural areas with a total coverage of around 20,000 km². The spatial resolution of the optical images is 2.5 m, and the pixel spacing of the SAR images is 1.25 m. To have a consistent pixel spacing within the image pairs, we downsampled the SAR images to 2.5 m using bilinear interpolation.

As the ground truth, we are using optical images which were aligned to the corresponding SAR images in the Urban Atlas project [52]. The alignment between the images was achieved by a manual selection of several hundred matching points for every image pair. These matching points are used to improve the sensor model related to the optical images. By using the improved sensor models to orthorectify the optical images, the global alignment error could be reduced from up to 23 m to around 3 m in this project.

To minimize the impact of the different acquisition modes of PRISM and TerraSAR-X, we focus on flat surfaces where only the radiometry between the SAR and optical images is different. Therefore, patches are favored that contain parts of streets or runways in rural areas. The patches are pre-selected using the CORINE land cover [53] from the year 2012 to exclude patches, e.g., containing street segments in city areas. The CORINE layer includes 44 land cover classes and has a pixel size of 100 m. For the pre-selection, the following classes are chosen: airports, non-irrigated arable land, permanently-irrigated land, annual crops associated with permanent crops and complex cultivation patterns, land principally occupied by agriculture, with significant areas of natural vegetation. Note that there are several current global land cover maps available, which enable a similar pre-selection for images outside Europe. The pre-selection was refined manually to ensure that the patches contain streets/runways segments that are visible in the optical and the SAR patches and to avoid patches containing street segments through smaller villages or areas covered by clouds in the optical images.

3.1. Dataset Generation

The training, validation and test datasets are generated by randomly splitting the 46 images into 36 images for training, 4 for validation and 6 for testing. As a form of data augmentation, we use bilinear interpolation to downsample the optical and SAR images, which are used for training, to a pixel spacing of 3.75 m. This leads to a training set with a total number of 92 images for each sensor, where half of the images have a resolution of 2.5 m and the other half of 3.75 m. Data augmentation is commonly used to generate a larger training dataset and, hence, to prevent the network from overfitting.

The training, validation and test patches are cropped from the images of the corresponding sets. The optical patches have a size of 201 × 201 pixels, and the SAR patches have a size of 221 × 221 pixels. The final dataset contains 135,000 pairs of training patches, 5000 pairs of validation patches and 14,400 pairs of test patches, and the total number of search locations is 441. Note that the alignment

error between the SAR and the optical image is expected to be not larger than 32 m. Therefore, a 21×21 pixel search space with a pixel spacing of 2.5 m in the validation and test case is assumed to be large enough.

3.2. Training Parameters

Our network is trained with 100 rounds, where each round takes 200 iterations over a single batch. The initial learning rate is set to 0.01, and we reduce it by a factor of five at iterations 60 and 80. We train the network in parallel on two Titan X GPUs using a batch size of 100. The weights of the network are initialized with the scheme described in [54], which particularly considers the rectifier nonlinearities. The whole training process takes around 30 h.

3.3. Influence of Speckle Filtering

To find the right setup, we investigated the influence of speckle filtering during training time. Figure 4a illustrates the matching accuracy of the validation set during training with two different network architectures and with and without the speckle filter. Here, the matching accuracy is measured as the percentage of matching points, where the Euclidean (L_2) distance to the ground truth location is less than or equal to 3 pixels. Figure 4b illustrates the average L_2 distance of the matching points to the ground truth location of the validation set in the training. Both images reveal that, independently from the network architectures, speckle filtering helps the network at learning the similarity between optical and SAR patches and, hence, at improving the accuracy of the generated matching points.

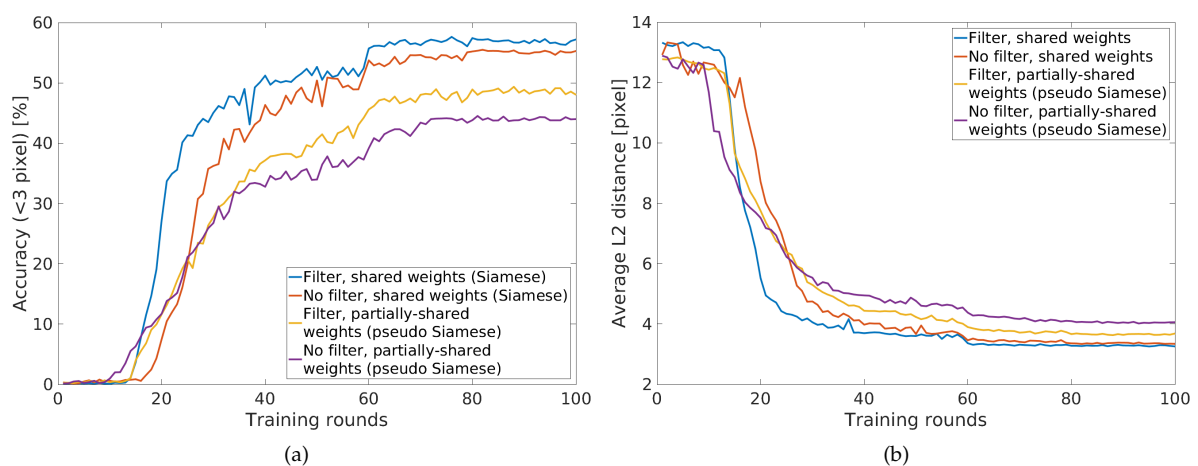


Figure 4. Influence of the speckle filter and comparison of different network architectures during training time (all results are generated from the validation set): (a) shows the matching accuracy during training. Here, the matching accuracy is measured as the percentage of matching points, where the L_2 distance to the ground truth location is less than or equal to three pixels; (b) shows the average L_2 distance between the matching points and the ground truth location during training.

3.4. Comparison of Network Architectures

The influence of partially-shared (pseudo-Siamese architecture) and shared weights (Siamese architecture) between the two network branches during training was investigated. In the case of the pseudo-Siamese architectures, the weights of the first three layers are different, whereas the remaining layers share their weights. In the case of the Siamese architectures, all weights are shared. Figure 4 shows a comparison of the matching accuracy between the results of Siamese and pseudo-Siamese architecture over the validation set. It can be seen that a full Siamese architecture learns slightly faster and achieves higher matching accuracy in the end. In the following, the results are generated with the best setup: speckle filtering combined with a Siamese architecture.

3.5. Comparison to Baseline Methods

For a better evaluation of our results, we compare our method with three available baseline methods: the similarity measure normalized cross-correlation (NCC) [55], the similarity measure mutual information (MI) [56], and a MI-based method (CAMRI) which is tailored to the problem of optical and SAR matching [10]. To ensure a fair comparison, we applied the pre-processing with the speckle filter [48] to all baseline methods, except for CAMRI [10]. Here, a slightly different speckle filter is implemented internally. Table 1 shows the comparison of our method with the baseline methods. The expression “Ours (score)” denotes our method, where we used a threshold to detect outliers and to generate more precise and reliable matching points (detailed explanation in the next section). “Ours (scores)” achieves higher matching accuracy and precision than NCC, MI and CAMRI [10]. More precisely, the average value over the L_2 distances between the matching points and the ground truth locations is the smallest (measured in pixel units) for our method. Furthermore, the comparison of the matching precisions reveals that our matching points, with a standard deviation σ of 1.14 pixels, are the most reliable ones. The running time of our method during test time is 3.3 m for all 14,000 test patches on a single GPU. The baseline methods are running on CPU, which makes a fair comparison difficult, but CAMRI [10] requires around three days to compute the matching points for the test set.

Table 1. Comparison of the matching accuracy and precision of our method with accuracies of normalized cross-correlation (NCC), mutual information (MI) and CAMRI [10] over the test set. The matching accuracy is measured as the percentage of matching points, having a L_2 distance to the ground truth location smaller than a specific number of pixels and as the average over the L_2 distances between the predicted matching points and the ground truth locations (measured in pixel units). The matching precision is represented by the standard deviation σ (measured in pixel units).

| Methods | Matching Accuracy | | | | Matching Precision | |
|--------------|-------------------|-----------|-----------|-------------------|--------------------|--|
| | <2 pixels | <3 pixels | <4 pixels | avg L_2 (pixel) | σ (pixel) | |
| NCC | 2.94% | 7.92% | 13.01% | 9.92 | 4.04 | |
| MI | 18.18% | 38.60% | 51.99% | 4.89 | 3.64 | |
| CAMRI [10] | 33.55% | 57.06% | 79.93% | 2.80 | 2.86 | |
| Ours | 25.40% | 49.60% | 64.28% | 3.91 | 3.17 | |
| Ours (score) | 49.70% | 82.80% | 94.70% | 1.91 | 1.14 | |

3.6. Outlier Removal

So far, we used the normalized score (after applying the soft-max) and we selected the locations with the highest value (highest probability) within each search area as the predicted matching point after a two-dimensional shift. Another possibility is to use the raw score (before soft-max) as an indicator of the confidence of the prediction. Utilizing this information, we can aggregate the predictions from the network to detect outliers and achieve higher matching performances. Therefore, we investigated the influence of the raw score as a threshold as shown in Figure 5, which enables the detection of correct predicted matching points. A higher threshold on the raw score leads to a better accuracy in terms of correct prediction, as well as a smaller L_2 distance between the predicted matching points and the ground truth locations. Note that the rough shape at the right side of the curves in Figure 5b,c is the result of an outlier. Here, an outlier has a strong influence, since these numbers are computed from less than 20 test patches.

By using only the first 1000 matches with the highest raw score, the average over the L_2 distances between the matching points and the ground truth location can be reduced from 3.91 pixels (using all matches) to 1.91 pixels, and the standard deviation (matching precision) from 3.37 to 1.14 pixels (see Table 1). Note that a higher threshold results in a smaller number of valid matching points, which are more reliable (in terms of the L_2 distance). For a later application, a threshold does not have to

be specified. Depending on the number of matching points x needed for an image pair, the best x matching points can be chosen, based on the raw score.

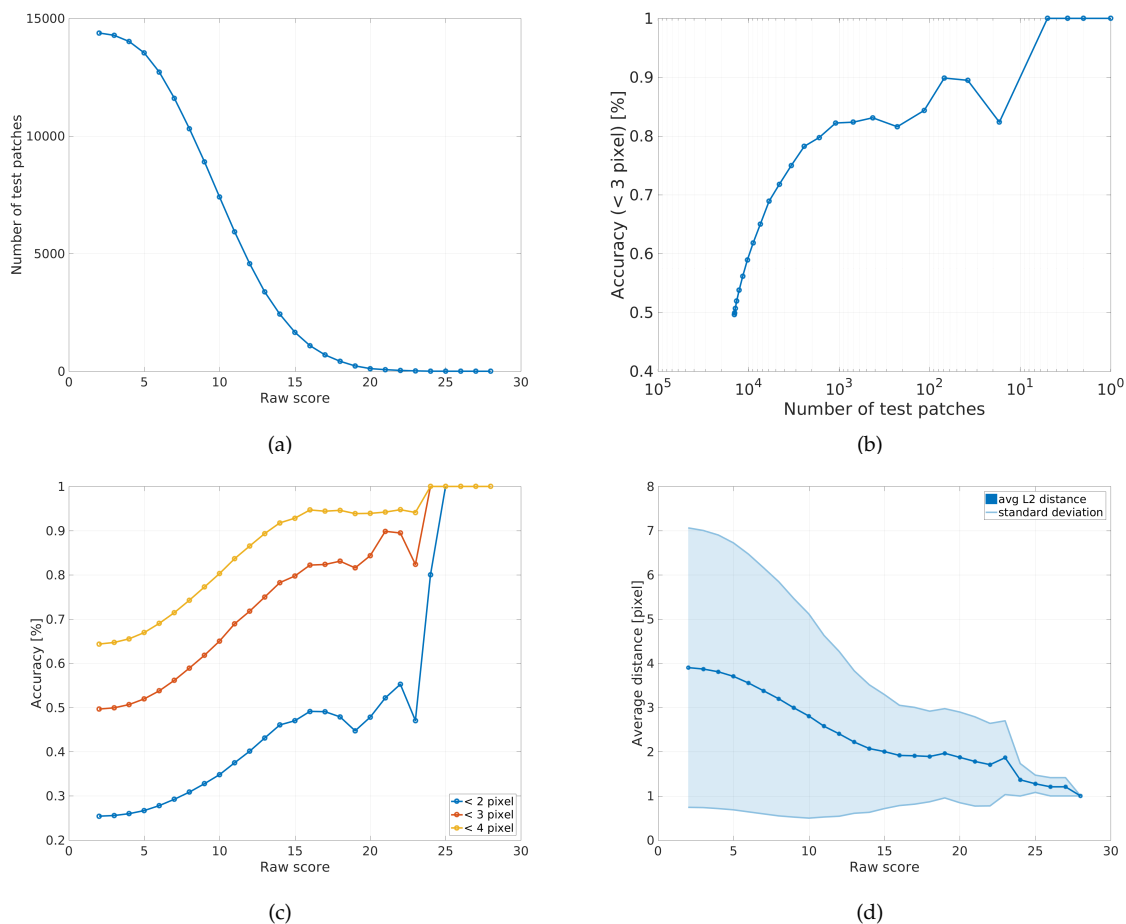


Figure 5. Illustration of influence of the raw score as a threshold: (a) the relation between the predicted score and the number of patches; (b) relation between the number of patches and the matching accuracy; (c) relation between the predicted score and the matching accuracy; and (d) relation between the predicted score and the average distance (L_2) between the predicted matching points and the ground truth location. The matching accuracy in Figure 5b is measured as the percentage of matching points, where the L_2 distance to the ground truth location is less than three pixels and in Figure 5c less than 2, 3 and 4 pixels.

3.7. Qualitative Results

In Figure 6, we show a side by side comparison of the score maps of our approach with two baseline methods of sample image patches. Note that CAMRI [10] does not provide a score map as output. Therefore, we perform our search over a 51×51 pixels search space, where the used patches have a resolution of 2.5 m. The images in the first column are optical image patches and the images in the last column the despeckled SAR image patches. To generate the images in column 2 to 4 we perform the matching between the corresponding image pairs using NCC, MI and our method. Yellow indicates a higher score, and blue indicates a lower score. The ground truth location is in the center of each patch. Our approach performs consistently better than the corresponding baseline methods. More precisely, the score maps generated with our approach show one high peak at the correct position, except for the last example. Here, two peaks are visible along a line, which corresponds to a street in the SAR patch. In contrast, both baseline methods show a relatively large area with a constantly high score at the wrong positions for most examples.

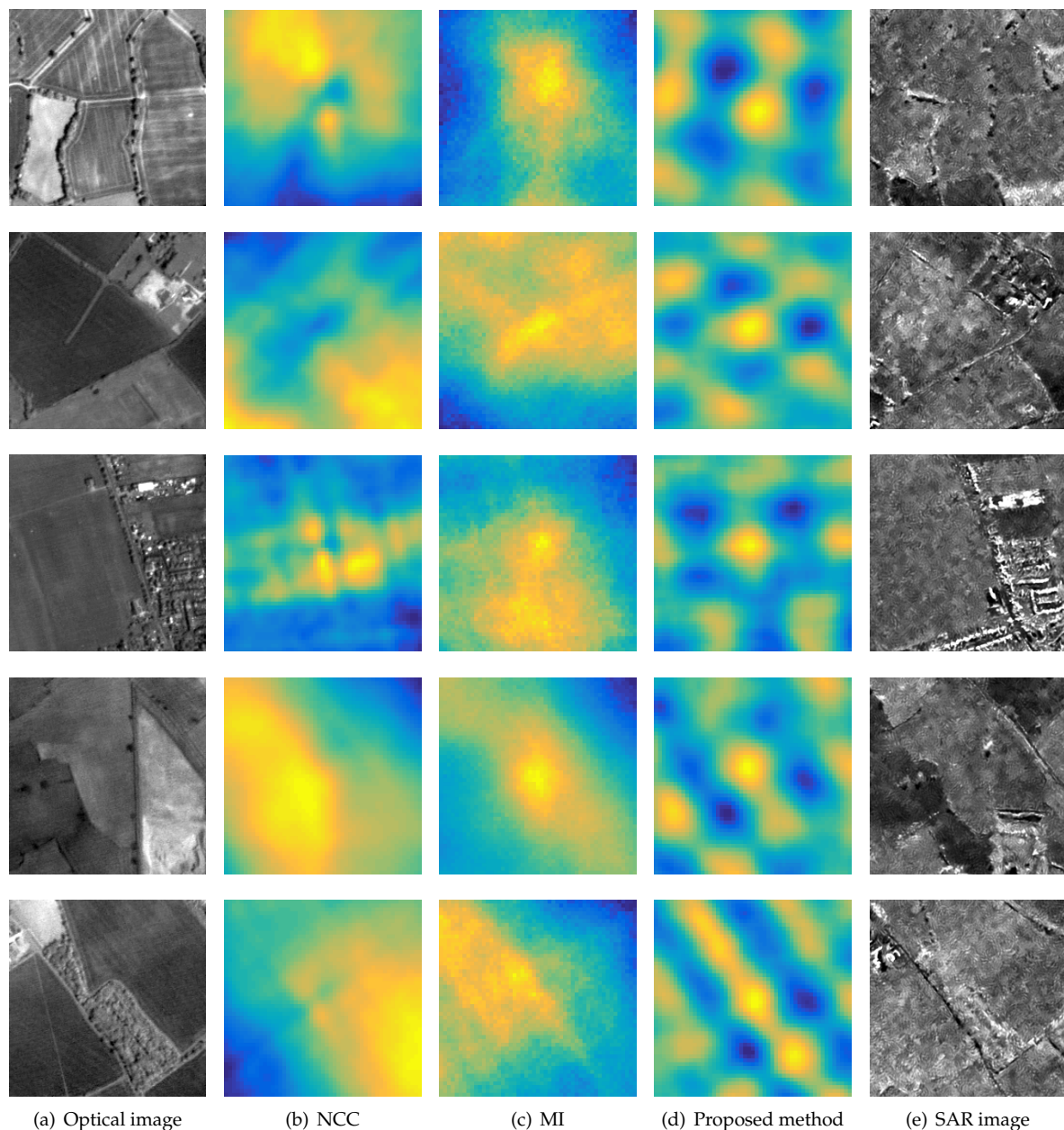
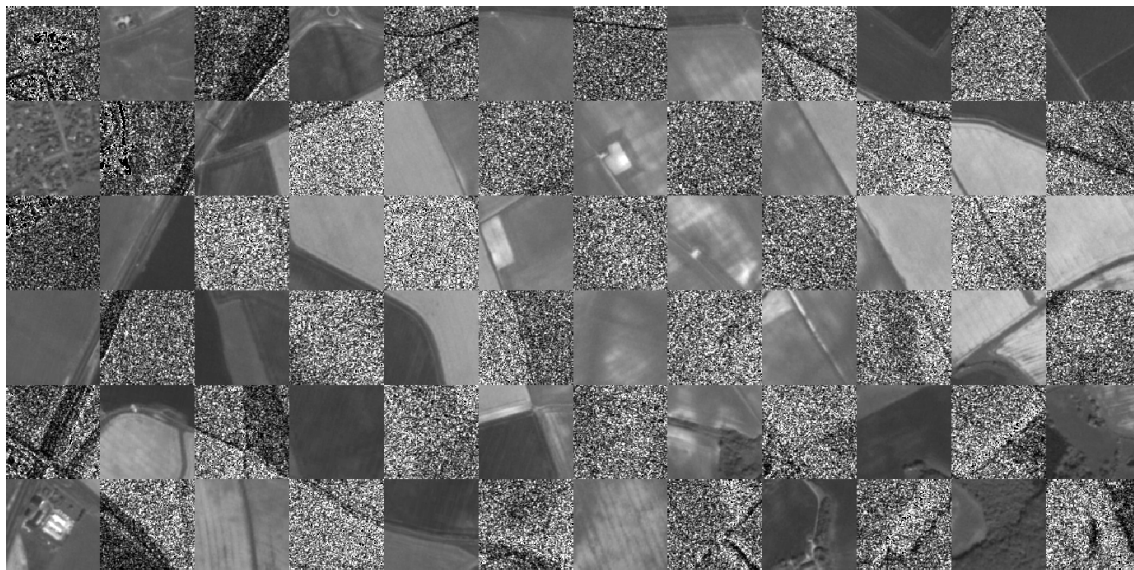


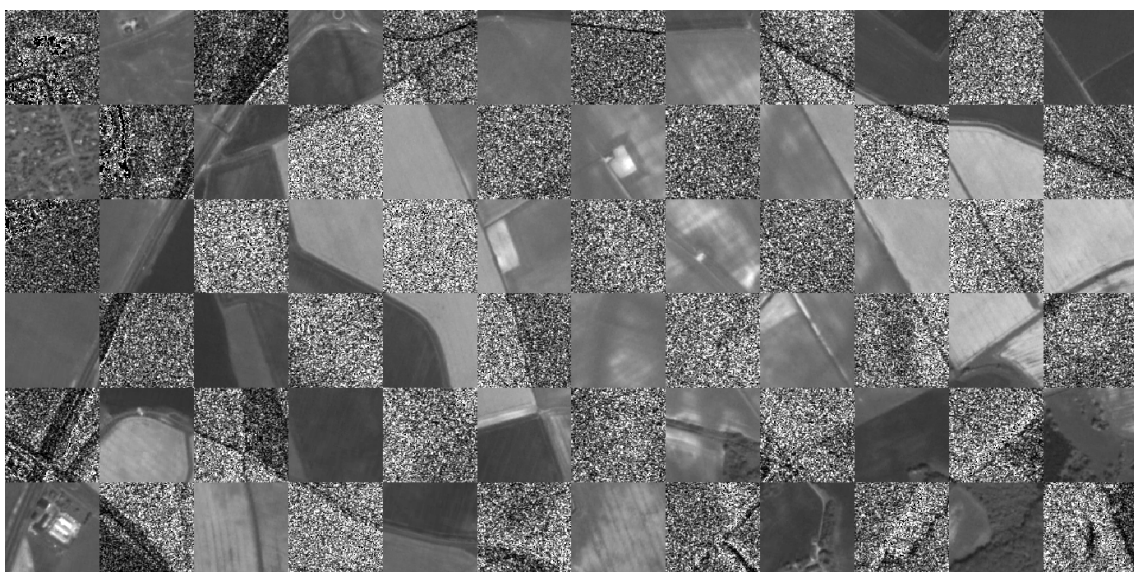
Figure 6. Side by side comparison between (a) optical patches (201×201 pixels), (b) the score maps of NCC, (c) MI, and (d) our method (51×51 pixels), and (e) the reference despeckled SAR patches (251×251 pixels).

In Figure 7, the checkerboard overlay of two optical and SAR image pairs is shown. The residual alignment error between the uncorrected optical and SAR images is clearly visible in the easting direction in Figure 7a. In contrast, the corrected optical and SAR image pair in Figure 7b seems to be aligned. For the correction of the optical image, we used the obtained matching points from the neural network to improve the parameters of the corresponding sensor model and, hence, to improve the geo-location accuracy. In particular, we picked the best 153 matching points (with the highest raw score and with at least a L_2 spatial distance of 50 pixels to each other) as our ground control points (GCPs). We set the empirical distance threshold to 50 pixels to ensure that the points are equally spread over the whole image. Afterwards, the unknown parameters of the sensor model are estimated from these GCPs by iterative least squares adjustment. During this process, a blunder detection removed 11

GCPs. At the end, we used the improved sensor model to generate a new orthorectified optical image with improved absolute geo-localization accuracy. The standard deviation for the remaining 142 GCPs is 1.04 pixels in the easting and 1.28 pixels in the northing direction.



(a) Before the geo-localization enhancement of the optical image.



(b) After the geo-localization enhancement of the optical image.

Figure 7. Checkerboard overlays of two optical and one SAR image with a pixel spacing of 2.5 m and image tiles size of 100×100 m: (a) shows the optical image before and (b) after the sensor model adjustment (geo-localization enhancement) through the generated matching points.

3.8. Limitations

A drawback of the current network architecture is the restriction to input patches of size 201×201 pixels for the left branch of the network. If we were to use the full resolution of the SAR images and upsample the optical images to 1.25 m, our training and test dataset would contain a large amount of image patches, containing just one straight line (street segment). These patches are ambiguous for our two-dimensional search and, hence, not suitable for the training process. As a consequence, we need larger image patches to reduce the amount of ambiguity. Therefore, we downsampled the optical and

SAR images. Due to the memory limits of our available GPUs, it was not possible to increase the input patch size and simultaneously keep a proper batch size. A possible solution could be the investigation of a new network architecture, which enables the use of larger input patches. An alternative solution could be a better selection process of the patches, e.g., only patches containing street crossings.

The processing chain for the generation of our dataset and the relatively small amount of training data represent the main current weaknesses. The selection of the image patches for the dataset was mainly done manually and is limited to one SAR and optical satellite sensor (PRISM and TerraSAR-X). Through the usage of OpenStreetMap and/or a road segmentation network, the generation of the dataset could be done automatically, and our datasets could be quickly extended with new image patches. A larger dataset would help to deal with the problem of overfitting during training, and further improve the network performance.

Additionally, the success of our approach depends on the existence of salient features in the image scene. To generate reliable matching points, these features have to exhibit the same geometric properties in the optical and SAR image, e.g., street-crossings. Therefore, the proposed method is not trained to work on images without such features, e.g., images covering only woodlands, mountainous areas or deserts.

3.9. Strengths

The results prove the potential of our method for the task of geo-localization improvement of optical images through SAR reference data. By interpreting the raw network output as the confidence for predicted matching points (predicted shifts) between optical and SAR patches, we are able to generate matching points with high matching accuracy and precision. Furthermore, the high quality of the matching points does not increase the computation time. After training, we can compute new matching points between arbitrary optical and SAR image pairs within seconds. In contrast, a MI-based approach like CAMRI [10] needs several hours or days to compute the matching points between the same image patches, yielding in less accurate and precise results.

In contrast to other deep learning-based matching approaches, our network is able to match multi-sensor images with different radiometric properties. Our neural network is extendible to images from other optical or radar sensors with little effort, and it is applicable to multi-resolution images. In contrast to other feature-based matching approaches, our method is based on reliable (in terms of equal geometric properties in the optical and SAR image patches) features, e.g., streets and street crossings, which frequently appear in many satellite images. Furthermore, through the variety in our training image pairs, our method is applicable to a wide range of images acquired over different countries or at different times of the year.

4. Conclusions

In this paper, the applicability of a deep learning-based approach for the geo-localization accuracy improvement of optical satellite images through SAR reference data is confirmed for the first time. For this purpose, a neural network has been trained to learn the spatial shift between optical and SAR image patches. The network is composed of a feature extraction part (Siamese network) and a similarity measure part (dot product layer). The network was trained on 134,000 and tested on 14,000 pairs of patches cropped from optical (PRISM) and SAR (TerraSAR-X) satellite image pairs over 13 city areas spread over Europe.

The effectiveness of our approach for the generation of accurate and reliable matching points between optical and SAR images patches has been demonstrated. Our method outperforms state-of-the-art matching approaches, like CAMRI [10]. Particular, matching points can be achieved with an average L_2 distance to the ground truth locations of 1.91 pixels and a precision (standard deviation) of 1.14 pixels. Furthermore, by utilizing the resulting improved sensor model for the geo-referencing and orthorectification processes, we achieve an enhancement of the geo-localization accuracy of the optical images.

In the future, we will further enhance the accuracy and precision of the resulting matching points by using interpolation or polynomial curve fitting techniques to generate sub-pixel two-dimensional shifts. Additionally, we are planning to investigate the influence of alternative network architectures, similarity measures and loss functions on the accuracy and precision of the matching points, as well as the applicability of an automatic processing chain for the dataset generation using OpenStreetMap and a road detection network.

Acknowledgments: We gratefully thank Mathias Schneider for helping with the generation of our dataset, Gerald Baier for helping with the pre-processing of the TerraSAR-X images and Peter Schwind for his valuable suggestions and support during the whole process.

Author Contributions: Nina Merkle, Wenjie Luo, Stefan Auer, Rupert Müller and Raquel Urtasun conceived and designed the experiments. Nina Merkle and Wenjie Luo wrote the source code. Nina Merkle generated the dataset, performed the experiments and wrote the paper. Wenjie Luo, Stefan Auer, Rupert Müller and Raquel Urtasun provided detailed advice during the writing process. Rupert Müller and Raquel Urtasun supervised the whole process and improved the manuscript.

Conflicts of Interest: The authors declare no conflict of interest.

References

1. Werninghaus, R.; Buckreuss, S. The TerraSAR-X Mission and System Design. *IEEE Trans. Geosci. Remote Sens.* **2010**, *Vol. 48*, pp. 606–614.
2. Eineder, M.; Minet, C.; Steigenberger, P.; Cong, X.; Fritz, T. Imaging Geodesy- Toward Centimeter-Level Ranging Accuracy with TerraSAR-X. *IEEE Trans. Geosci. Remote Sens.* **2011**, *Vol. 49*, pp. 661–671.
3. Reinartz, P.; Müller, R.; Schwind, P.; Suri, S.; Bamler, R. Orthorectification of VHR Optical Satellite Data Exploiting the Geometric Accuracy of TerraSAR-X Data. *ISPRS J. Photogramm. Remote Sens.* **2011**, *Vol. 66*, pp. 124–132.
4. Cumming, I.; Wong, F. *Digital Processing of Synthetic Aperture Radar Data: Algorithms and Implementation*; Number Bd. 1 in Artech House Remote Sensing Library; Artech House Inc., Boston, London, **2005**.
5. Auer, S.; Gernhardt, S. Linear Signatures in Urban SAR Images—Partly Misinterpreted? *IEEE Geosci. Remote Sens. Lett.* **2014**, *Vol. 11*, pp. 1762–1766.
6. Merkle, N.; Müller, R.; Reinartz, P. Registration of Optical and SAR Satellite Images based on Geometric Feature Templates. *ISPRS - International Archives of the Photogrammetry, Remote Sensing and Spatial Information Sciences*, *Vol. XL-1/W5*, **2015**, pp. 447–452.
7. Perko, R.; Raggam, H.; Gutjahr, K.; Schardt, M. Using Worldwide Available TerraSAR-X Data to Calibrate the Geo-location Accuracy of Optical Sensors. In *Proceedings of the 2011 IEEE International Geoscience and Remote Sensing Symposium, IGARSS, Vancouver, BC, Canada, 24–29 July 2011*; pp. 2551–2554.
8. Shi, W.; Su, F.; Wang, R.; Fan, J. A Visual Circle Based Image Registration Algorithm for Optical and SAR Imagery. In *Proceedings of the 2012 IEEE International Geoscience and Remote Sensing Symposium, Munich, Germany, 22–27 July 2012*; pp. 2109–2112.
9. Siddique, M.A.; Sarfraz, M.S.; Bornemann, D.; Hellwich, O. Automatic Registration of SAR and Optical Images Based on Mutual Information Assisted Monte Carlo. In *Proceedings of the 2012 IEEE International Geoscience and Remote Sensing Symposium, Munich, Germany, 22–27 July 2012*; pp. 1813–1816.
10. Suri, S.; Reinartz, P. Mutual-Information-Based Registration of TerraSAR-X and Ikonos Imagery in Urban Areas. *IEEE Trans. Geosci. Remote Sens.* **2010**, *Vol. 48*, pp. 939–949.
11. Hasan, M.; Pickering, M.R.; Jia, X. Robust Automatic Registration of Multimodal Satellite Images Using CCRE with Partial Volume Interpolation. *IEEE Trans. Geosci. Remote Sens.* **2012**, *Vol. 50*, pp. 4050–4061.
12. Inglada, J.; Giros, A. On the Possibility of Automatic Multisensor Image Registration. *IEEE Trans. Geosci. Remote Sens.* **2004**, *Vol. 42*, pp. 2104–2120.
13. Liu, X.; Lei, Z.; Yu, Q.; Zhang, X.; Shang, Y.; Hou, W. Multi-Modal Image Matching Based on Local Frequency Information. *EURASIP J. Adv. Signal Process.* **2013**, pp. 1–11.
14. Li, Q.; Qu, G.; Li, Z. Matching Between SAR Images and Optical Images Based on HOG Descriptor. In *Proceedings of the Radar Conference 2013, IET International, Xi'an, China, 14–16 April 2013*; pp. 1–4.

15. Ye, Y.; Shen, L. HOPC: A Novel Similarity Metric Based on Geometric Structural Properties for Multi-modal Remote Sensing Image Matching. *ISPRS Ann. Photogramm. Remote Sens. Spat. Inf. Sci.* **2016**, Vol. III-1, pp. 9–16.
16. Hong, T.D.; Schowengerdt, R.A. A Robust Technique for Precise Registration of Radar and Optical Satellite Images. *Photogramm. Eng. Remote Sens.* **2005**, Vol. 71, pp. 585–593.
17. Li, H.; Manjunath, B.S.; Mitra, S.K. A Contour-Based Approach to Multisensor Image Registration. *IEEE Trans. Image Process.* **1995**, Vol. 4, pp. 320–334.
18. Pan, C.; Zhang, Z.; Yan, H.; Wu, G.; Ma, S. Multisource Data Registration Based on NURBS Description of Contours. *Int. J. Remote Sens.* **2008**, Vol. 29, pp. 569–591.
19. Dare, P.; Dowman, I. An Improved Model for Automatic Feature-Based Registration of SAR and SPOT Images. *ISPRS J. Photogramm. Remote Sens.* **2001**, Vol. 56, pp. 13–28.
20. Long, T.; Jiao, W.; Hea, G.; Zhanga, Z.; Chenga, B.; Wang, W. A Generic Framework for Image Rectification Using Multiple Types of Feature. *ISPRS J. Photogramm. Remote Sens.* **2015**, Vol. 102, pp. 161–171.
21. Fan, B.; Huo, C.; Pan, C.; Kong, Q. Registration of Optical and SAR Satellite Images by Exploring the Spatial Relationship of the Improved SIFT. *IEEE Geosci. Remote Sens. Lett.* **2013**, Vol. 10, pp. 657–661.
22. Xu, C.; Sui, H.; Li, H.; Liu, J. An Automatic Optical and SAR Image Registration Method with Iterative Level Set Segmentation and SIFT. *Int. J. Remote Sens.* **2015**, Vol. 36, pp. 3997–4017.
23. Sui, H.; Xu, C.; Liu, J.; Hua, F. Automatic Optical-to-SAR Image Registration by Iterative Line Extraction and Voronoi Integrated Spectral Point Matching. *IEEE Trans. Geosci. Remote Sens.* **2015**, Vol. 53, pp. 6058–6072.
24. Han, Y.; Byun, Y. Automatic and Accurate Registration of VHR Optical and SAR Images Using a Quadtree Structure. *Int. J. Remote Sens.* **2015**, Vol. 36, pp. 2277–2295.
25. Chen, Y.; Lin, Z.; Zhao, X.; Wang, G.; Gu, Y. Deep Learning-Based Classification of Hyperspectral Data. *Sel. Top. Appl. Earth Obs. Remote Sens. IEEE J.* **2014**, Vol. 7, pp. 2094–2107.
26. Liang, H.; Li, Q. Hyperspectral Imagery Classification Using Sparse Representations of Convolutional Neural Network Features. *Remote Sens.* **2016**, Vol. 8(2), 99.
27. Wang, Q.; Lin, J.; Yuan, Y. Salient Band Selection for Hyperspectral Image Classification via Manifold Ranking. *IEEE Trans. Neural Netw. Learn. Syst.* **2016**, Vol. 27, pp. 1279–1289.
28. Mnih, V.; Hinton, G.E. Learning to Detect Roads in High-Resolution Aerial Images. In *Computer Vision—ECCV 2010, Proceedings of the 11th European Conference on Computer Vision*, Heraklion, Crete, Greece, 5–11 September 2010; Springer: Berlin/Heidelberg, Germany, **2010**; Part VI, pp. 210–223.
29. Matthys, G.; Wang, S.; Fidler, S.; Urtasun, R. HD Maps: Fine-grained Road Segmentation by Parsing Ground and Aerial Images. In *Proceedings of the IEEE International Conference on Computer Vision (ICCV)*, Las Vegas, NV, USA, 27–30 June **2016**; pp. 3611–3619.
30. Geng, J.; Fan, J.; Wang, H.; Ma, X.; Li, B.; Chen, F. High-Resolution SAR Image Classification via Deep Convolutional Autoencoders. *Geosci. Remote Sens. Lett. IEEE* **2015**, Vol. 12, pp. 2351–2355.
31. Masi, G.; Cozzolino, D.; Verdoliva, L.; Scarpa, G. Pansharpening by Convolutional Neural Networks. *Remote Sens.* **2016**, Vol. 8, 594.
32. Luo, W.; Schwing, A.G.; Urtasun, R. Efficient Deep Learning for Stereo Matching. In *Proceedings of the IEEE Conference on Computer Vision and Pattern Recognition (CVPR)*, Las Vegas, NV, USA, 27–30 June **2016**.
33. Zbontar, J.; LeCun, Y. Stereo Matching by Training a Convolutional Neural Network to Compare Image Patches. *J. Mach. Learn. Res.* **2016**, Vol. 17, pp. 1–32.
34. Bai, M.; Luo, W.; Kundu, K.; Urtasun, R. Exploiting Semantic Information and Deep Matching for Optical Flow. In *Proceedings of the European Conference on Computer Vision (ECCV)*, Amsterdam, The Netherlands, 8–16 October **2016**.
35. Weinzaepfel, P.; Revaud, J.; Harchaoui, Z.; Schmid, C. DeepFlow: Large Displacement OpticalFlow with Deep Matching. In *Proceedings of the IEEE International Conference on Computer Vision (ICCV)*, Sydney, Australia, 1–8 December **2013**.
36. Altwaijry, H.; Trulls, E.; Hays, J.; Fua, P.; Belongie, S. Learning to Match Aerial Images with Deep Attentive Architectures. In *Proceedings of the IEEE Conference on Computer Vision and Pattern Recognition (CVPR)*, Las Vegas, NV, USA, 27–30 June **2016**.
37. Lin, T.Y.; Cui, Y.; Belongie, S.; Hays, J. Learning Deep Representations for Ground-to-Aerial Geolocalization. In *Proceedings of the IEEE Conference on Computer Vision and Pattern Recognition (CVPR)*, Boston, MA, USA, 7–12 June **2015**.

38. Altwaijry, H.; Veit, A.; Belongie, S. Learning to Detect and Match Keypoints with Deep Architectures. *In Proceedings of the British Machine Vision Conference (BMVC)*, York, UK, 19–22 September 2016.
39. Bromley, J.; Guyon, I.; LeCun, Y.; Säckinger, E.; Shah, R. Signature Verification using a “Siamese” Time Delay Neural Network. *In Proceedings of the Conference on Neural Information Processing Systems (NIPS)*, Denver, Colorado, USA, 28 Nov.–1 December 1994.
40. Vincent, P.; Larochelle, H.; Lajoie, I.; Bengio, Y.; Manzagol, P.A. Stacked Denoising Autoencoders: Learning Useful Representations in a Deep Network with a Local Denoising Criterion. *J. Mach. Learn. Res.* **2010**, Vol. 11, pp. 3371–3408.
41. Fischer, A.; Igel, C. An Introduction to Restricted Boltzmann Machines. *In Progress in Pattern Recognition, Image Analysis, Computer Vision, and Applications, Proceedings of the 17th Iberoamerican Congress, CIARP 2012, Buenos Aires, Argentina, 3–6 September 2012*; Springer: Berlin/Heidelberg, Germany, 2012; pp. 14–36.
42. Krizhevsky, A.; Sutskever, I.; Hinton, G.E. ImageNet Classification with Deep Convolutional Neural Networks. *In Proceedings of the Advances in Neural Information Processing Systems (NIPS)*, Lake Tahoe, USA, 3–8 December 2012.
43. Han, X.; Leung, T.; Jia, Y.; Sukthankar, R.; Berg, A.C. MatchNet: Unifying Feature and Metric Learning for Patch-Based Matching. *In Proceedings of the IEEE Conference on Computer Vision and Pattern Recognition (CVPR)*, Boston, MA, USA, 7–12 June 2015.
44. Zagoruyko, S.; Komodakis, N. Learning to Compare Image Patches via Convolutional Neural Networks. *In Proceedings of the IEEE Conference on Computer Vision and Pattern Recognition (CVPR)*, Boston, MA, USA, 7–12 June 2015.
45. Simo-Serra, E.; Trulls, E.; Ferraz, L.; Kokkinos, I.; Fua, P.; Moreno-Noguer, F. Discriminative Learning of Deep Convolutional Feature Point Descriptors. *In Proceedings of the International Conference on Computer Vision (ICCV)*, Santiago, Chile, 11–18 December 2015.
46. Yu, F.; Koltun, V. Multi-Scale Context Aggregation by Dilated Convolutions. *In International Conference on Learning Representations (ICLR)*, San Juan, Puerto Rico, 2–4 May 2016.
47. Ioffe, S.; Szegedy, C. Batch Normalization: Accelerating Deep Network Training by Reducing Internal Covariate Shift. *In Proceedings of the 32nd International Conference on Machine Learning (ICML), JMLR Workshop and Conference Proceedings*, Lille, France, 6–11 July 2015, pp. 448–456.
48. Deledalle, C.; Denis, L.; Tupin, F. Iterative Weighted Maximum Likelihood Denoising with Probabilistic Patch-Based Weights. *IEEE Trans. Image Process.* **2009**, Vol. 18, pp. 2661–2672.
49. Buades, A.; Coll, B. A Non-Local Algorithm for Image Denoising. *In Proceedings of the IEEE Conference on Computer Vision and Pattern Recognition (CVPR)*, San Diego, CA, USA, 20–26 June 2005.
50. Kingma, D.; Ba, J. Adam: A Method for Stochastic Optimization. *arXiv* **2014**, arXiv:1412.6980.
51. Müller, R.; Krauß, T.; Schneider, M.; Reinartz, P. Automated Georeferencing of Optical Satellite Data with Integrated Sensor Model Improvement. *Photogramm. Eng. Remote Sens.* **2012**, Vol. 78, pp. 61–74.
52. Schneider, M.; Müller, R.; Krauß, T.; Reinartz, P.; Hörsch, B.; Schmuck, S. Urban Atlas—DLR Processing Chain for Orthorectification of PRISM and AVNIR-2 Images and TerraSAR-X as possible GCP Source. *In Proceedings of the International Proceedings: 3rd ALOS PI Symposium*, Kona, USA, 09–13 November 2009; pp. 1–6.
53. Bossard, M.; Feranec, J.; Otahel, J. *CORINE Land Cover Technical Guide—Addendum 2000*; European Environmental Agency, Copenhagen, Denmark, 2000.
54. He, K.; Zhang, X.; Ren, S.; Sun, J. Delving Deep Into Rectifiers: Surpassing Human-Level Performance on ImageNet Classification. *In Proceedings of the IEEE International Conference on Computer Vision (ICCV)*, Santiago, Chile, 11–18 December 2015.
55. Burger, W.; Burge, M.J. *Principles of Digital Image Processing: Core Algorithms, 1st ed.*; Springer Publishing Company, Incorporated, London, England, 2009.
56. Walters-Williams, J.; Li, Y., Estimation of Mutual Information: A Survey. *In Rough Sets and Knowledge Technology, Proceedings of the 4th International Conference (RSKT)*, Gold Coast, Australia, 14–16 July 2009; Springer: Berlin/Heidelberg, Germany, 2009; pp. 389–396.

